ARTICLE IN PRESS

Ceramics International xxx (xxxx) xxx-xxx

FISEVIER

Contents lists available at ScienceDirect

Ceramics International

journal homepage: www.elsevier.com/locate/ceramint



Enhanced electrochemical performance of graphene aerogels by using combined reducing agents based on mild chemical reduction method

Ramin Shadkam^{a,b}, Malek Naderi^{a,b,*}, Arash Ghazitabar^{a,b}, Armin Asghari-Alamdari^{a,b}, Sara Shateri^{a,b}

ARTICLE INFO

Keywords: Graphene aerogel Mild reduction Ascorbic acid Sodium bisulfite electrochemical capacitance

ABSTRACT

In recent years, 3D assemblies of graphene are developed as promising materials in various applications, such as energy storage devices. In this paper, we have reported a method for the synthesis of Graphene Aerogel (GA) utilizing a novel reducing system to achieve high electrochemical properties. GAs were obtained via chemical reduction of Graphene Oxide (GO) using a combination of L-Ascorbic Acid (L-AA) and sodium bisulfite (NaHSO₃) as the combined reduction media (GASL). However, L-AA exhibited a high level of reduction resulting in a micro/mesoporous structure, but it is incapable of de-epoxidation with high efficiency. Besides, NaHSO₃ enhanced the de-epoxidation step, decreased the shrinkage of the structure, and also increased the size of the pores. The synergistic effect of the combined reducing system led to the proper level of reduction with meso/macroporous structure and lowered shrinkage, which improved the electrochemical performance. The N₂ adsorption analysis with BET formula estimated the specific surface area and the pore volume of 135 m²g⁻¹ and 2.9 cm³g⁻¹, respectively. Moreover, FT-IR spectroscopy admitted a high level of reduction for GASL in comparison with single reducing agent samples. The GASL exhibited a high specific capacitance (165 Fg⁻¹ at 1 Ag⁻¹), excellent cycling stability (91% capacitance retention after 1000 cycles) and an adequate capacitive performance (91% capacitance retention by the increase in current density from 1 to 5 Ag⁻¹) with low internal resistance (about 0.005 V). The desired results are due to the high level of reduction and the meso/macroporous structure.

1. Introduction

Graphene, this one-atom-thick lattice of carbon atoms, presents exceptional properties, which are strongly connected to the production route. The defects of the graphene sheets and the issue of restacking have weakened the perfect characteristics of ideal graphene, especially electrical properties and high surface area. To dispel these drawbacks, 3-Dimensional (3D) monoliths are developed. The assemblies of graphene sheets into 3D structures not only maintain the fundamental properties of graphene, but also endow the benefits of high accessible surface area, interconnected channels, adjustable pore structure, and less aggregation [1–3].

The main procedures developed to obtain these arranged structures are based on direct gelation and self-assembly of functionalized graphene sheets. The preparation of aerogels mostly occurs by a wet chemical route such as sol-gel reaction but through different precursors and conditions. In most researches, GO is the precursor material for the synthesis of 3D graphene structures. GO sheets can attach to form a 3D

structure via either reduction, adding a cross-linking agent, or by increasing the concentration of GO [4–6].

The chemical and hydrothermal reduction are the most-cited methods to produce graphene monolith from GO suspension. In comparison with relatively elevated temperatures and pressures used in thermal reduction, the chemical route carries out at low temperatures. As a result, the equipment and conditions of chemical reduction are much more available than thermal reduction, which has got undeniable importance for practical applications [7–11].

The products of the chemical reduction route are strongly dependent on the solvent and reducing agent employed in the reaction. Up to this point, dozens of reducing agents have been introduced and exploited, including L-ascorbic acid (LAA), hydrazine or hydrazine hydrate, sodium borohydride (NaBH4), sodium hydroxide (NaOH), and hydroiodic acid (HI) [12]. Although sodium bisulfite (NaHSO₃) has been used as a reductant in some of the studies [12–14], this material is mostly employed as a catalyst in functionalization reactions such as amination [15].

https://doi.org/10.1016/j.ceramint.2020.05.297

Received 4 April 2020; Received in revised form 25 May 2020; Accepted 28 May 2020 0272-8842/ © 2020 Elsevier Ltd and Techna Group S.r.l. All rights reserved.

^a Department of Materials and Metallurgical Engineering, Amirkabir University of Technology, Iran

^b Graphene and Advanced Materials Laboratory (GAMLab), Tehran, Iran

^{*} Corresponding author. Department of Materials and Metallurgical Engineering, Amirkabir University of Technology, 15875-4413, Iran. E-mail address: mnaderi@aut.ac.ir (M. Naderi).

L-Ascorbic acid, also known as vitamin C, having a gentle ability of reduction and non-poisonous property, is naturally used as a reducing agent. LAA and its oxidized products are more environmentally friendly than the other reducing agents, such as hydrazine. Zhang and coworkers reported that using LAA as a reducing agent could provide graphene aerogels for 48 h, also using a higher concentration of vitamin C was able to decrease the reduction time [16]. Also, Chen et al. used a variety of sulfur-containing components, including sodium bisulfite, and compared their reduction performance to other reductants [17]. The results showed that NaHSO₃ has equal reduction efficiency as hydrazine. On the other hand, GO reduced by NaHSO₃ exhibited better electrical conductivity performance, about 27% more than ones reduced by hydrazine [12,14,17].

As mentioned, graphene aerogels possess lots of excellent properties such as high specific surface area, low density, and excellent conductivity, which made them excellent candidates for electrode material of supercapacitors. On the other hand, the graphitic electrodes cannot be functionalized due to the tendency for restacking [18]. Recently, Wu et al. have exploited graphene paper (GP) for preparing electrodes and obtained 57 Fg $^{-1}$ capacitance which was improved by additives [19]. Furthermore, Ghazitabar et al. made electrodes from graphene aerogel, which was reduced just by LAA and achieved 71 Fg $^{-1}$ capacitance [20]. Bi et al. synthesized an electrode of carbon nanotube/graphene aerogel on the Cu substrate and obtained 42.3 Fg $^{-1}$ capacitance at the current density of 1 Ag $^{-1}$ [21]. All the findings show that 3D graphene opens a new avenue for modifying batteries and supercapacitors [22–26].

Herein, we developed a new combined system which is composed of L-AA and NaHSO $_3$ acting as reducing agents. The role of NaHSO $_3$ in the reduction process and the corresponded effect on the pore structure have been investigated. The enhancement of mechanical stability of synthesized Graphene Hydrogel (GH) and Aerogel (GA) was discussed through the exploration of surface chemistry of rGO sheets and the pore structure. Accurately, the electrochemical performance of the best sample has been characterized and compared to some of the reported results in the literature.

2. Materials and methods

2.1. Materials

Graphite powder, sodium nitrate (NaNO₃), and potassium permanganate 97% (KMnO₄) were provided from Dae-Jung (Korea). $_{\rm L}$ -Ascorbic Acid powder, sodium bisulfite, HCl (37%), $_{\rm H_2}$ SO₄ (98%), $_{\rm H_2}$ O₂ (30%) were purchased from Merck Co. (Germany).

2.2. GO preparation

GO was prepared according to Hummers' method. Briefly, 5 g of graphite powder and 2.5 g of sodium nitrate were added into 115 mL of concentrated sulfuric acid. Then 25 g of potassium permanganate was added slowly, while keeping the system at the temperatures lower than 10 °C for 25 min. The well-mixed suspension was heated to 35 °C and kept for 45 min to form a thick mixture. After adding 140 mL of double-distilled water, the temperature of the mixture was increased to 98 °C for another 45 min, where the color of the mixture changed from brown to yellow. Subsequently, 30 mL of hydrogen peroxide ($\rm H_2O_2$) was added. The obtained mixture was filtered and washed with diluted HCl solution (10% v/v). Finally, the mixture was centrifuged several times at 10,000 rpm until the pH of the system reached to neutral.

2.3. GA preparation

A mixture of LAA and NaHSO $_3$ was added to GO suspension as the reducing system. The mass ratio of GO to the reducing mixture was set at 1:5, and the mass ratio of LAA to NaHSO $_3$ was set at 1:1 (each of the reducing agents makes 50% of the mixture). The GA100L and GA100S

Table 1
Samples reduced by different reducing agents.

Sample	Ascorbic acid	Sodium bisulfite
GAL	100%	-
GASL	50%	50%
GAS	-	100%

samples were synthesized using only LAA and only NaHSO $_3$ as reducing agents, respectively. At a temperature of 90 °C (in an oil bath), the GHs were formed after 4 h. Afterward, the as-prepared GHs were washed by double-distilled water to remove unreacted species. After 24 h of freezedrying, the hydrogels were transformed into aerogel. The composition of the samples are presented in Table 1.

2.4. Electrochemical tests

Electrodes have been prepared using Ghazitabar et al. method [20]. Electrochemical characterizations such as Cyclic Voltammetry (CV), Galvanostatic Charge-Discharge (GCD), and Electrochemical Impedance Spectroscopy (EIS) were conducted by the ZIVE electrochemical measurement apparatus. A three-electrode system comprised of a Pt plate as the counter electrode and Ag/AgCl as the reference electrode was exploited, using 2 M KOH aqueous electrolyte. The specific capacitance was calculated from the discharge curves according to the following equation:

$$C = \frac{I \times \Delta t}{m \times \Delta V}$$

Where C (Fg⁻¹) is the specific capacitance of electrodes, I (A) is the discharge current, Δt (s) is the discharge time, m (g) is the mass of the active material, and ΔV is the potential window [27].

For the evaluation of the electrochemical capacitance, GCD analysis is a reliable method under the adjusted current situation. In this technique, the current is controlled and the voltage is computed. The specific capacitance calculated using this method is entirely different from cyclic voltammetry since the numerical estimation of capacitance from the surface within CV graphs can cause errors in calculations.

2.5. Characterization

The hydrogel samples were dried via the freeze-drying method using an FD-10V freeze-drier apparatus (Tajhizat Sazan Pishtaz Co., Iran). Philips XL 30 device was used to take scanning electron microscopy (SEM) images. Transmission electron microscopy (TEM) was performed on a Philips CM-200 FEG to observe the size and shape of the graphene sheets. X-Ray Diffraction (XRD) patterns was recorded on a Philips X-ray powder diffractometer system with Cu K α radiation ($\lambda = 1.5418$ Å) operated at 40 kV and 150 mA, at a scanning step of 0.04° and the scanning angle from 5° to 80°. A Fourier transform infrared spectroscopy (FTIR) Thermo AVATAR model was used to measure chemical bonds and functional groups. The electrical conductivity of graphene aerogels was measured using the standard four-probe method by scientific equipment & Services Company. The resulting errors in this measurement were estimated to be less than 5%.

3. Results and discussion

3.1. Morphology & microstructure

To observe the morphology of the graphene sheets within the 3D structure, SEM and TEM analysis are exploited. As is evident in Fig. (1-4), the as-prepared aerogels have a 3D porous structures comprised of an interconnected network of channels. These channels are essential to make rGO sheets accessible, since the mass transfer for each kind of species e.g. ions and molecules, takes place through these paths. The

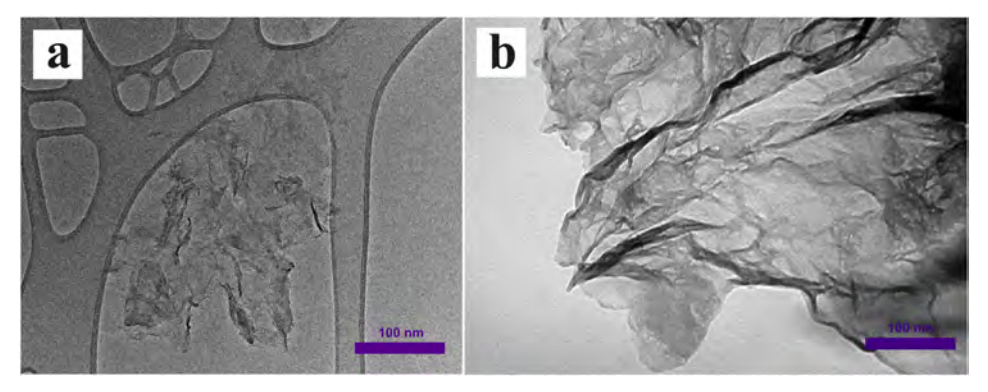


Fig. 1. TEM images of wrinkled rGO sheets.

wrinkled rGO sheets with dimensions in the range of a few microns are illustrated in Fig. 1. During the self-assembly process, these layered components organized the cell walls of the pore structure.

As is shown in Fig. 2(a–b), GAS pore sizes are in the range of macropores due to the weaker cross-linking effect of sodium bisulfite, as a reducing agent. This structure has many voids and closed pores which caused the decrement in the electrochemical properties. Fig. 2(c–d) also shows the pore structure of the GAL sample. The mesopores and macropores are formed due to the participation of ascorbic acid in the hydrogel-formation process. In this case, by-products of L-AA oxidation are bound to the remaining oxygen-functionalities and play the role of cross-linking in the 3D graphene structure, which will be further discussed in the following sections [16]. The open porestructure with the high surface area makes GAL desirable for electrochemical applications.

For the GASL sample, the combination of ascorbic acid and sodium bisulfite as reducing agents resulted in a different pore-structures. Although the structure of the channels remained the same, with the partial decrement in the size of the pores the GASL can be concluded as a meso/macroporous structure without any voids (Fig. 3).

 $\rm N_2$ adsorption analysis was employed to evaluate the pore structure of the synthesized aerogels. Based on the adsorption-desorption

isotherms, the specific surface area of the GASL sample is calculated $135\ m^2g^{-1}$ and the total pore volume around 2.9 cm $^3\ g^{-1}$. Due to the formation of more macropores and macroscopic voids, the specific surface area for GAL and GAS are measured $81\ m^2g^{-1}$ and $75\ m^2g^{-1}$, respectively [28]. It means the agglomeration and restacking of rGO sheets have been successfully minimized during the reduction, as a result of the utilization of both reducing agents.

Pore volume and the mean pore radius of all three samples showed a rational correlation with SEM images (Figs. 1 and 2). Table 2 indicates some of the structural properties of the samples, including bulk density. The density of GASL stands between GAS and GAL, which have the lowest and the highest densities, respectively. GAS has the lowest density due to the macroporous structure and the lowest shrinkage during the hydrogel-formation step. In the GAL sample, the compact mesoporous structure with high shrinkage caused the increase in the bulk density. GASL showed an intermediate shrinkage which resulted in a moderate bulk density in comparison with GAL and GAS samples.

The phase structure of the samples was examined through the X-ray Diffraction (XRD) method. XRD patterns of GO, GAL, GAS, and GASL samples are shown in Fig. 4.

As shown in Fig. 4, the typical diffraction peak for GO appeared at $2\theta = 11.43^{\circ}$ attributed to the (001) diffraction planes and interlayer

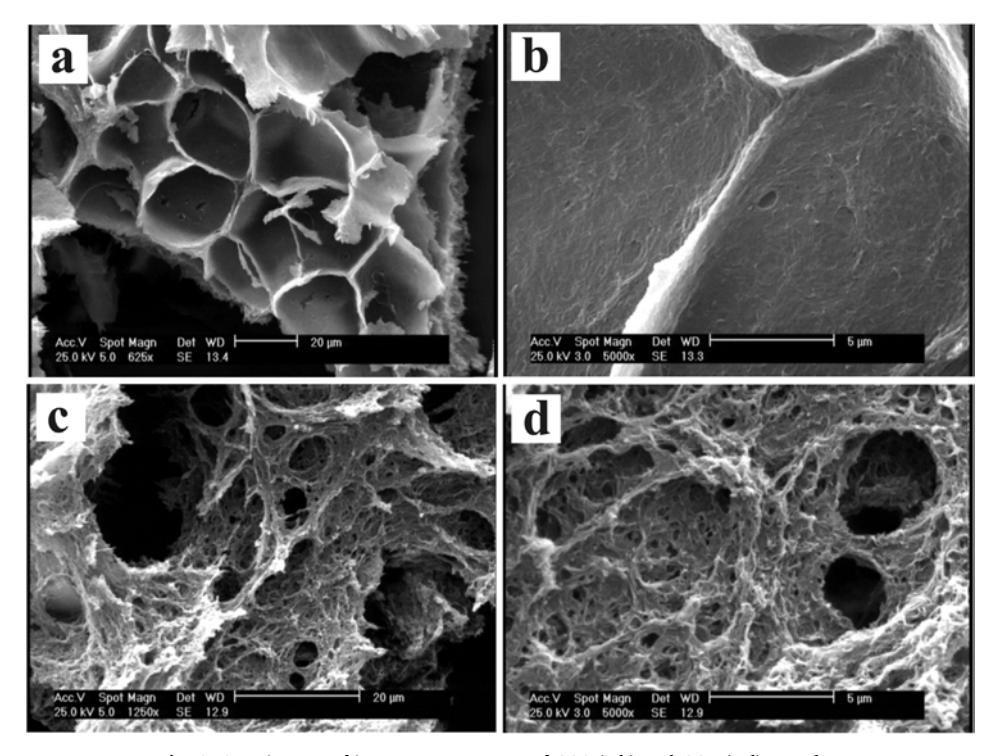


Fig. 2. SEM images of inner pore structure of GAS (a,b) and GAL (c,d) samples.

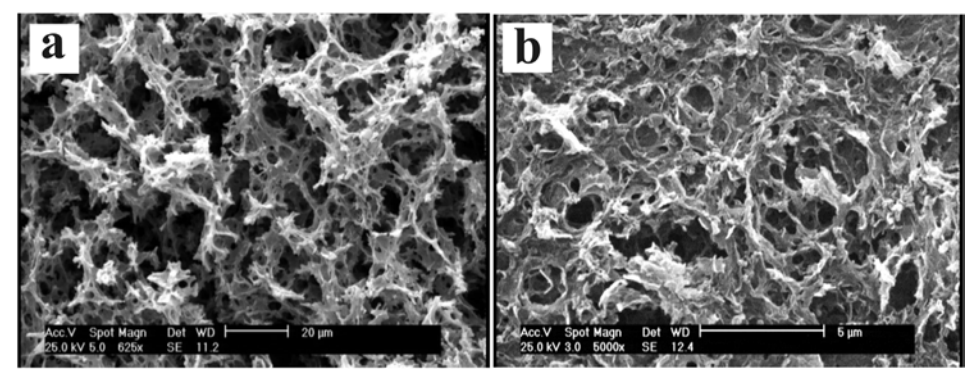


Fig. 3. SEM images of inner pore structure of GASL sample in two magnifications.

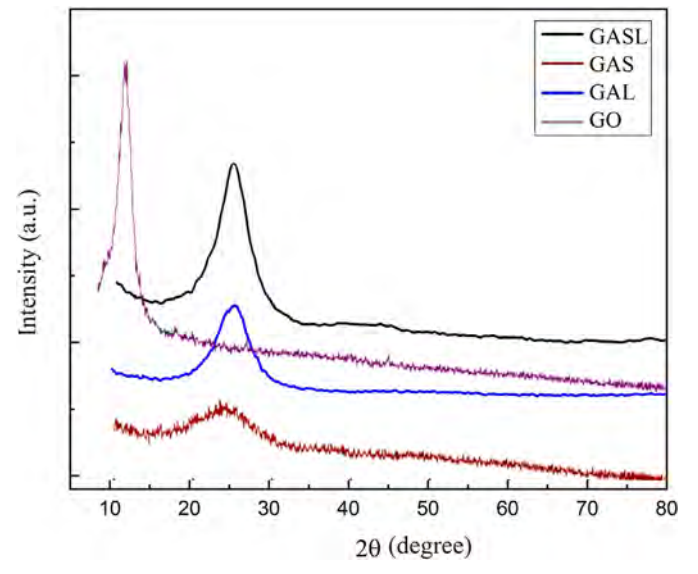


Fig. 4. XRD patterns of GO, GAS, GAL and GASL samples.

space (d) of 7.76 Å. After reduction, the partial removal of the oxygencontaining groups on GO sheets and the increase in π - π interactions between rGO sheets resulted in a decrease in interlayer space. Therefore, the sharp peak of GO disappeared and shifted to a broad peak at around $2\theta = 23.5^{\circ}$ corresponded to interlayer space of 3.4, 3.55, and 3.5 Å for GAS, GAL, and GASL, respectively. All of the patterns, after the reduction, are so close to the typical peak of (002) diffraction planes of graphite with interlayer space of 3.35 Å at $2\theta = 26.6^{\circ}$ [30–32]. XRD spectra of GASL showed a higher peak intensity in comparison with GAL and GAS due to the higher boundary defect density which is formed in the hydrogel-formation process. Another reason for the highest peak intensity is the high level of reduction in the GASL sample [3,33,34]. For a better evaluation of the reduction level in aerogel samples, FTIR analysis was performed.

Qualitative amount of functional groups on GO sheets, before and after the reduction, can be studied through the assessment of relative intensities of peaks corresponded to the oxygen-containing functional

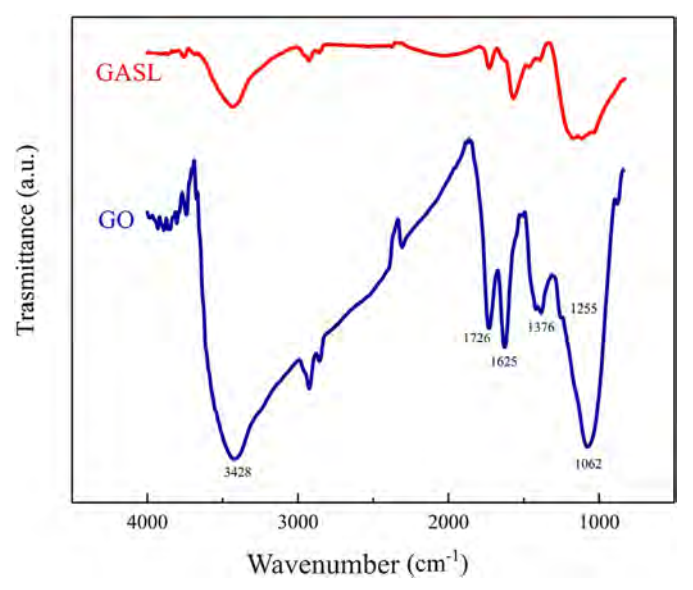


Fig. 5. FTIR spectra of GO and GASL.

groups. Fig. 5 demonstrates the FTIR spectra of GO and GASL samples. The characteristic absorption peaks for GO appeared at 1726 cm⁻¹ representing stretching vibration peak of C=O bond in carbonyl and carboxylic acid groups, 1062 cm⁻¹ attributed to C-O bonds in alkoxy and carboxyl groups, and 1255 cm⁻¹ corresponded to C-O-C bond in epoxy groups. Moreover, there are peaks at 3428 and 1376 cm⁻¹ contributed to stretching and bending vibrations of O-H bonds in hydroxyl and carboxyl groups, respectively [3,32,35,36]. As we expected, the oxygen-containing functionalities such as carbonyl and epoxy groups showed a severe decline in intensity after the reduction. Even the peak corresponded to hydroxyl groups was disappeared. In contrast, the absorption peak of the C=C bonds of the graphene basal planes, which appeared at 1625 cm⁻¹, showed no significant change in the rGO spectrum. The characteristic peaks of GO and GA samples are briefly presented in Table 3.

The effect of LAA, NaHSO $_3$, and the combined system on the removal of oxygen-containing groups is illustrated in Fig. 6.

Table 2 Physical properties of samples; pore structure characteristics.

Sample	Specific surface area (m ² g ⁻¹)	Mean pore radius (nm)	Pore volume (cm ³ g ⁻¹)	Density (mg cm ⁻¹)	Ref.
GO	136	_	_	-	[28]
rGO	98	_	1.9	_	[29]
GAS	75	8	0.6	8.8	This work
GAL	81	1	1.22	23.2	This work
GASL	135	5	2.9	16.1	This work
GASL	135	5	2.9	16.1	

Table 3 Characteristic FTIR peaks of GO.

Peak wavenumber (cm ⁻¹)	Functional Group
1726	C=0
1062	C-O
1255	C-O-C
3428	О-Н
1376	
1625	C = C

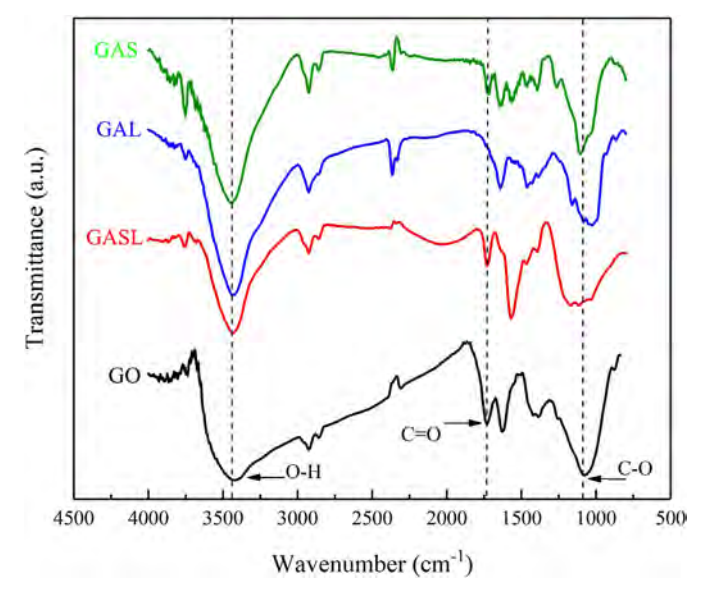


Fig. 6. FTIR spectra of all samples; GO, GAS, GAL and GASL.

The intensities of all the oxygen-containing moieties have an obvious decrease, but there are differences between the three spectra. As shown, the GAL spectrum shows total removal of the carbonyl peak at 1726 $\rm \,cm^{-1}$, meaning that LAA can remove carboxylic acid functionalities efficiently. In contrast, with the addition of NaHSO $_3$ the GASL spectrum demonstrates further reduction of the intensities in the range of 1050-1100 $\rm \,cm^{-1}$ contributed to the epoxy group. This fact implies that NaHSO $_3$ can enhance the de-epoxidation of GO sheets. Besides, the GASL spectrum shows a lower intensities of hydroxyl peaks at 1376 and 3428 $\rm \,cm^{-1}$ compared to GAS and GAL, which indicates the superior reduction efficiency of this complex reducing system.

To express the semi-quantitative Level of Reduction (LOR) of all samples, the sum of area under C-O (A_{1062}) and C=O (A_{1726}) bands are analyzed. The LOR can be calculated as the following equation:

$$LOR = \frac{1}{A_{1062} + A_{1726}}$$

In Table 4, the LOR values for different GA samples are expressed relative to the corresponded GO from which the aerogel is synthesized, for comparative purposes.

These results confirm that the principal reason for the highest peak intensity in the XRD pattern of the GASL sample is the recovery of more sp^2 regions due to the high level of reduction [9]. The electrical

Table 4The ratio of LOR of each graphene aerogel samples (GAs) system to that of GO.

Sample	$LOR = (A_{1062} + A_{1726})^{-1}$	LOR of GA/LOR of GO
GO	0.002	1
GAS	0.36	180
GAL	0.2	100
GASL	0.11	55

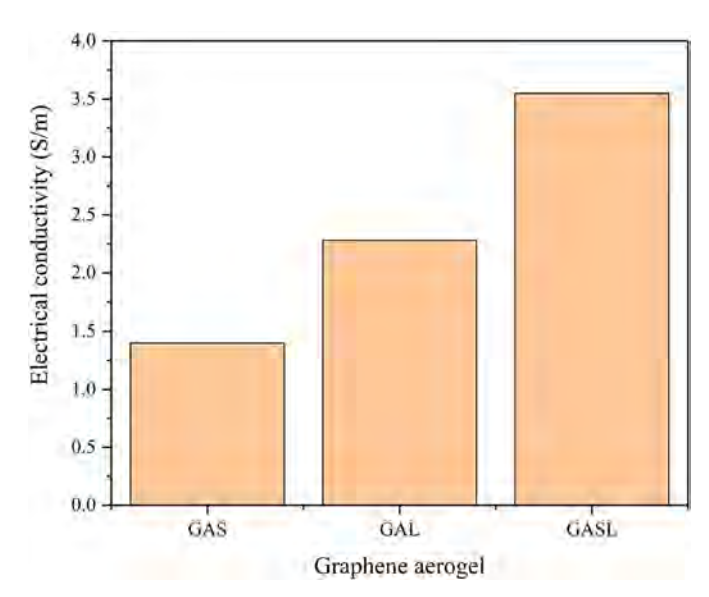


Fig. 7. The electrical conductivity of GAS, GAL, and GASL.

conductivity of the samples is shown in Fig. 7.

The electrical conductivity of GAS, GAL, and GASL are 1.4, 2.2 and 3.6 Sm⁻¹, respectively. FTIR and XRD results indicate that the incorporation of both reducing agents in the reduction process improved the electronic conductivity of graphene aerogel (GASL). In other words, as a result of improvement in the reduction and less aggregated sheets, a larger amount of carbon atoms that were engaged in the covalent bonds, are restored and contributing to the electronic conductivity.

3.2. Hydrogel formation

During the first stages of the reduction process, the chemical reaction between reducing agents and GO sheets leads to the gradual removal of the oxygen-containing groups. It is well known that the hydrophilic nature of GO sheets is a consequence of the presence of these functional groups. So as GO sheets start to lose these moieties, the hydrophilicity turns to hydrophobicity and the brown suspension changes to a black viscose pulp, as a result of deoxygenation. Then GO sheets isolate from water and form a closely packed structure, named rGO hydrogel. By the progression of the reaction, the increment in the level of reduction causes the enhancement of π - π interactions between conjugated rGO sheets, so hydrogel shrinks in dimensions. The suitable duration time for the reduction can be considered the time that the hydrogel gets fully packed and the shrinkage stops. In the final stage of the reduction reaction, a hydrogel that forms the shape of the vessel is floated on a clear solution [1,37].

As depicted in Fig. 8, both samples were isolated after 30 min in an oil bath, showing the reduction is on-going. After the completion, the hydrogels found to be in the same shape but different sizes. Fig. 8 demonstrated that GAS is the largest sample and GAL is the smallest in dimensions, although the volume of starting materials and the reduction times were equal. So from the final dimensions, this is obvious that the unary LAA reducing system has the most reduction rate amongst all. The lower reduction rate of NaHSO₃ can be an advantage, while the reduction via LAA results in vigorous bubble generation through deoxygenation. This phenomenon can cause real damage to the hydrogel structure and even lead to collapse. Fig. 9 demonstrates the effect of bubbling on structural stability during the reduction. To decrease this bubbling effect the reduction temperature has to be lessened, so the time needed for reduction via LAA will be much longer inevitably.

On the other hand, the reduction time needed to form the GAS hydrogel is a lot more than samples reduced via LAA. As mentioned before, all of the samples containing LAA in the reducing system have

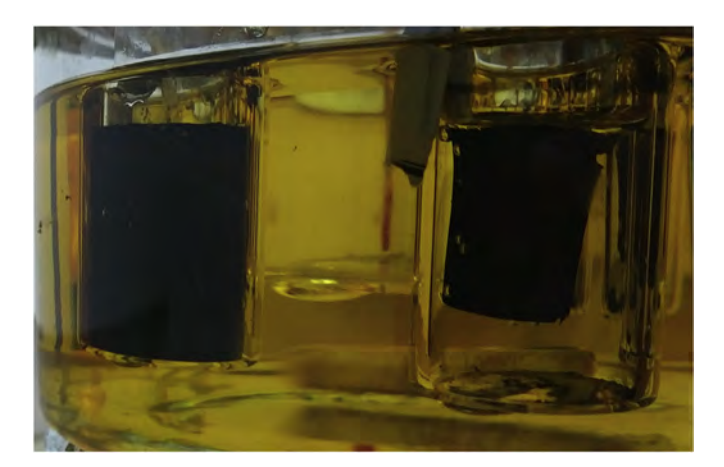


Fig. 8. Samples in oil bath during the reduction process; GAS (left) showed no significant changes in volume compared with GAL (right).



Fig. 9. The bubbling effect; GAL sample showed a large number of bubbles on the surface generated by gasses released during reduction.

been isolated from solution after 30 min and started the shrinkage, despite GAS which was isolated after 3 h and even at the final stage did not reach the other samples size.

The GAS sample has the lowest volume shrinkage in the hydrogel-forming process due to the presence of internal voids and macroporous structure. The volume shrinkage is 35% for GAS, while this parameter is 65% for the GAL sample because of the more mesopores. By decreasing the volume shrinkage, an aerogel with low density is expected. In the GASL sample, the volume shrinkage is moderate (about 50%) to make low-density aerogel which is suitable for electrode materials. In conclusion, a combination of both reducing agents causes the formation of low-density graphene aerogel with promising properties to use as electrode materials in electrochemical capacitors.

3.3. Reduction mechanism

The proposed mechanism for the oxidation of LAA molecules through the reduction process is based on the deprotonation of LAA molecules. Two protons (H⁺) are generated through this reaction, and ascorbic acid is converted to dehydroascorbic acid. On the other hand, carboxyl (-COOH) and hydroxyl (-OH) groups on the edge of the GO sheets can be deprotonated in neutral pH spontaneously [38]. These protons are very chemically active and able to reduce the oxygencontaining groups such as hydroxyl and epoxy functionalities, mostly located on basal planes of GO [16].

The catalytic role of NaHSO $_3$ has been discussed in different researches [15]. There are not many proposed reactions that illustrate the reduction mechanism using NaHSO $_3$ as a reductant. Chen et al. have suggested that the sulfur-containing reductants can open the epoxy ring and enhance the de-epoxidation step of the reduction. The primary mechanism occurs upon dissociation of NaHSO $_3$ in aqueous media and the production of HSO $_3$. These ions attack the C-O bond and replace it with the C-S bond. Then the free oxygen is ready to be protonated and release a water molecule. At the end of the reaction, SO $_3$ molecules are detached from reduced GO sheet and converted to soluble SO $_4$ ions, which can be easily washed out from the system. The process is shown schematically shown in Fig. 10. The fact that this material leaves no byproducts in the final hydrogel is highly beneficial [12,39].

The main reason behind the function of LAA as a reductant is the structural stability of the final product. This stability is originated from cross-linkage caused by LAA's by-products. Following the deprotonation of LAA molecules, dehydroascorbic acid transforms into oxalic and guluronic acid [16]. These species can form strong hydrogen bonds with residual oxygen-containing groups, which are remained on rGO sheets. This edge-by-edge connection is the crucial factor in achieving a robust 3D structure with high surface area, while they can prevent rGO sheets from restacking through face-to-face $\pi\text{-}\pi$ interactions. The schematic of the proposed reaction for cross-linkage is depicted in Fig. 11.

So it can be said that although NaHSO $_3$ can act as a reductant, it facilitates the reduction process through enhancement of the de-epoxidation step. The removal of each epoxy moiety on the edge of the GO plane can release two carbon atoms from the covalent bond and add them to the basal plane to contribute to the electrical conductivity. Moreover, the decrement in density due to high pore volume can ease the mass transfer of ions through the internal channels, which means more accessible and activated rGO sheets within the structure. As a result, we can expect enhanced electrochemical characteristics by the utilization of NaHSO $_3$.

3.4. Electrochemical performance

Cyclic Voltammetry (CV) is one of the adaptable electrochemical analyzes which is appropriate for electro-active samples. The CV test was conducted on all samples and as is obvious from Fig. 12, there is no

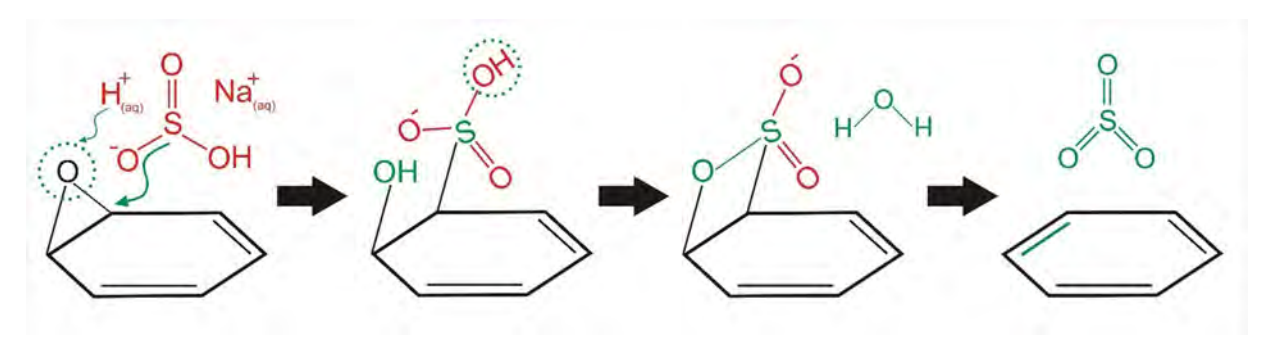


Fig. 10. The proposed role for $NaHSO_3$ in reduction process; ring-opening reaction.

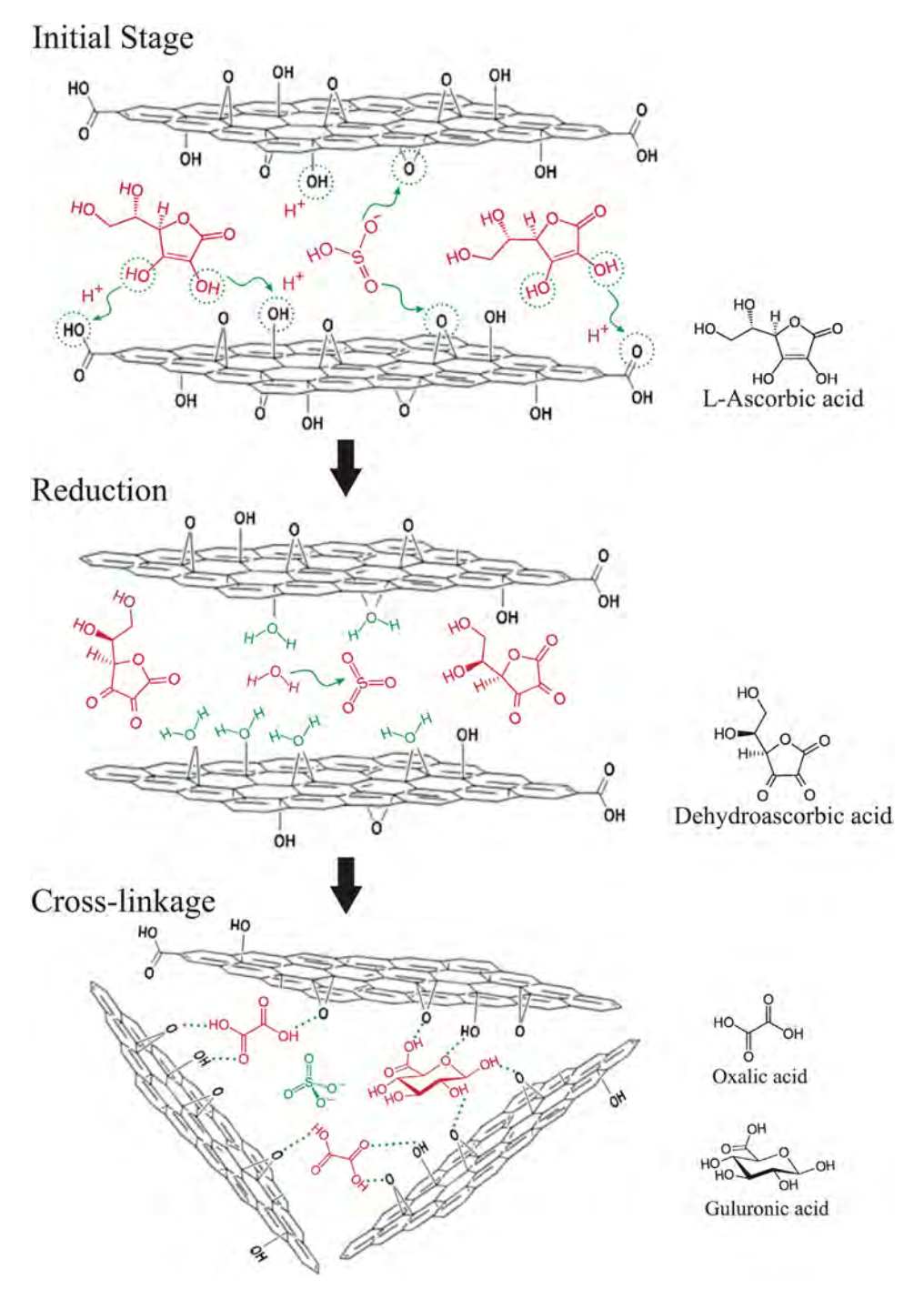


Fig. 11. Schematic of the reduction reaction and cross-linking effect.

sign of reduction and oxidation reactions in the curves.

The comparison of CV curves indicated the integral area of the GASL curve is more than the other samples, which ascribes a higher specific capacitance resulted from a structure with more porosity and more electrical conductivity. From the results obtained from the $\rm N_2$ adsorption test, GASL has a higher specific surface area (about 1.6 times higher than GAL and 1.8 times higher than GAS) which is in agreement with the CV curves. Furthermore, the higher pore volume of GASL causes the electrolyte ions to have further access to the active material and release higher adsorption/desorption electrolyte ions on graphene sheets and store higher energies. According to Fig. 13 which contains CV curves of the samples at scan rates of 10 mV/s and 50 mV/s, the rectangular and symmetric shapes of the CV curves remain the same

with an increase in scan rate and there is no noticeable change in the shape of GASL and GAL curves.

These observations can be indicative of cyclic stability and good reversibility of GASL and GAL samples due to their mesoporous structure. However, there is a slight change in the GAS curve by increasing the scan rate, as a result of aggregated sheets and less surface area which decreases reversibility. In the GAL sample, cross-linking caused a decrease in π - π interactions between graphene sheets and reduced the number of aggregated sheets in the 3D graphene structure.

For the estimation of the electrochemical capacitance, the Galvanostatic Charge-Discharge (GCD) test is a reliable route under the adjusted current situation. Using this method, parameters such as capacitance, resistance, and cyclability are concluded [40]. The GCD

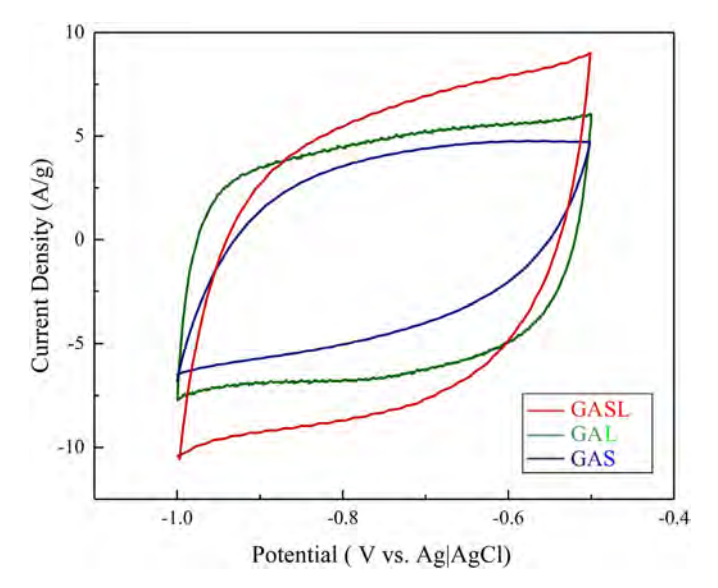


Fig. 12. Cyclic Voltammetry curves of the samples at the scan rate of 50 mV/s.

curves of the samples at current densities of 1 Ag⁻¹ and 5 Ag⁻¹ are shown in Fig. 14.

It is noticeable that the shape of each charge-discharge curve exhibits an excellent linear shape with a typical triangle symmetrical distribution that indicates sufficient columbic efficiency (an ideal capacitive behavior). Furthermore, Table 5 shows the specific capacitance of each sample at current densities of 5 Ag $^{-1}$ and 1 Ag $^{-1}$.

The decrease in specific current density will provide enough active sites for the ions to diffuse from the electrolyte into the pores and be transferred to the active sites to contribute to the electrochemical reactions. FTIR analysis showed that the level of reduction in the GASL sample was higher than the two other samples. This provides high electrical conductivity for GASL with fewer oxygen species that decrease the active sites for electrolyte ions.

As shown in Fig. 14, a dramatic voltage drop corresponding to the IR drop, is estimated to be 0.025 V for a current density of 5 ${\rm Ag}^{-1}$ and 0.005 V for 1 ${\rm Ag}^{-1}$ for the GASL electrode. IR drops of the GAS and GAL electrodes are higher than GASL due to higher aggregated graphene sheets and a lower level of reduction. This phenomenon happens due to the internal resistance of the material. Although it is worth mentioning that in comparison with other samples the resistance is the least, because of the combined reducing system resulted in the enhancement of the pore volume and preventing the agglomeration of graphene plates. Also, from the results of FTIR analysis GASL is reduced better than the others; this happens because of the presence of NaHSO3 that facilitates the removal of epoxy groups through ring-opening reaction which provides restoration of the conjugated structure. This fact is in

agreement with FTIR analysis, as mentioned before. As a result, more activated sites are enabled for incorporation in electrochemical reactions, and this results in the enhancement of electrochemical properties. Fig. 15 (a and b) shows the capacity retention of the GASL electrode after passing 1000 cycles charge/discharge at 1 Ag⁻¹ current density.

According to Fig. 15-a, the specific capacitance of GASL is calculated 165 Fg $^{-1}$, which demonstrates excellent cyclic capacitance stability after 1000 cycles. Furthermore, the capacitance is retained around 91%, reaching 150 Fg $^{-1}$ at the last cycle (Fig. 15-b). Table 6 is a comparison between the specific capacitance results of this work with others reported in the literature.

The capacitance retention of the GASL sample is measured at about 91%. This prominent result is obtained due to the enhanced pore structure of the graphene aerogel with a high level of reduction. As mentioned in the previous work [20] when LAA is just added as a reducing agent, pore volume is $0.2~{\rm cm^3g^{-1}}$. While the addition of NaHSO $_3$ combined with LAA led to a pore volume of $2.9~{\rm cm^3g^{-1}}$ which is about 14 times higher; this enhancement paves the way of more ion diffusion and charge transfer to the active materials.

Observations show that NaHSO $_3$ provides more pore volume than only using LAA as a reductant. The high specific surface area plays an important role in electrochemical performance; as there are more pores on the surface, the electrolyte can be transferred better, and as a result, ion conductivity is improved. Thus, if the porosities are on a microscopic scale, they will be blocked by the ions which have the same scale. Whereas larger channels can transfer the different sizes of ions more quickly. Ghazitabar et al. reported 71 Fg $^{-1}$ at 1 Ag $^{-1}$ for specific capacitance by using just LAA as a reducing agent [20]. Chen and Yan reported a specific capacitance of 156 Fg $^{-1}$ at a potential scan rate of 20 mV/s for NaHSO $_3$ reduced graphene oxide, but the result is not comparable while the calculation method was based on CV test [14]. So, the excellent electrochemical performance, such as high specific capacitance and high capacitance retention is obtained by using combined reducing agents for graphene aerogel synthesis.

Electrochemical Impedance Spectroscopy (EIS) includes quantification and examination of the materials with strong ionic conductivity. EIS test was conducted in the frequency range of 10 MHz to 100 kHz for an advanced study of the cycling stability (Fig. 16).

The semicircle region at the high-frequency range on the Nyquist plot is attributed to the interfacial resistance and the charge-transfer reactions. Also, the direct line in the low-frequency region is related to the Warburg line, which causes ions diffusion within an electrode and also a representative of the capacitive performance of the electrodes. The resistance of the solution occurs at the beginning of the semicircle, which indicates the electrolyte resistance. Besides, the electrochemical system is described by a Randles equivalent circuit (Fig. 16-b), consisting of an electrolyte resistance (R_s) in series with a parallel combination of double-layer capacitance (C_{cl}) and charge transfer resistance (R_{cl}), and the Warburg element (Z_w) taking diffusion into account.

The charge transfer resistance (R $_{ct}$) is estimated at 0.2 Ω from the

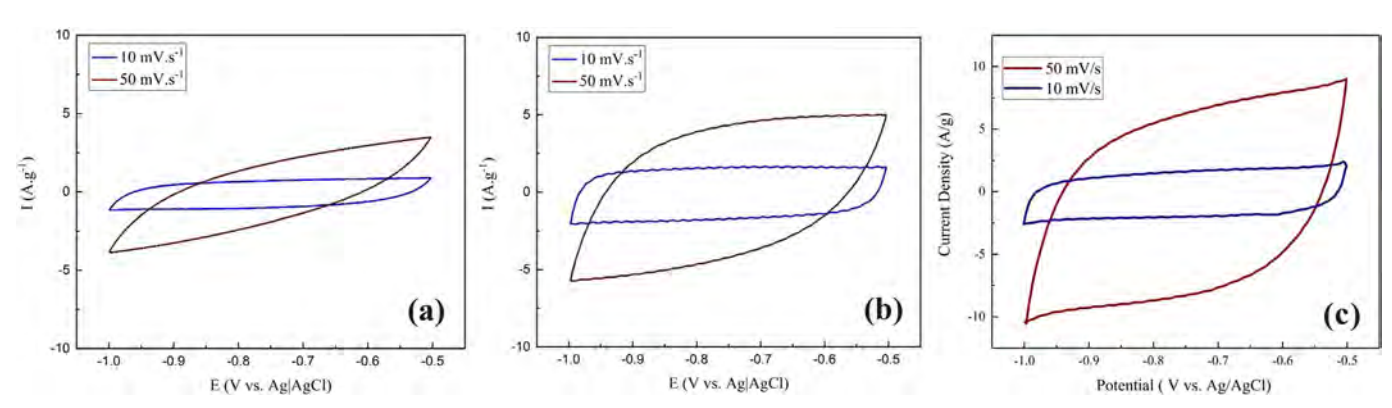


Fig. 13. Cyclic voltammetry curves of a) GAS, b) GAL and c) GASL samples measured at a scan rate of 10 mV/s and 50 mV/s.

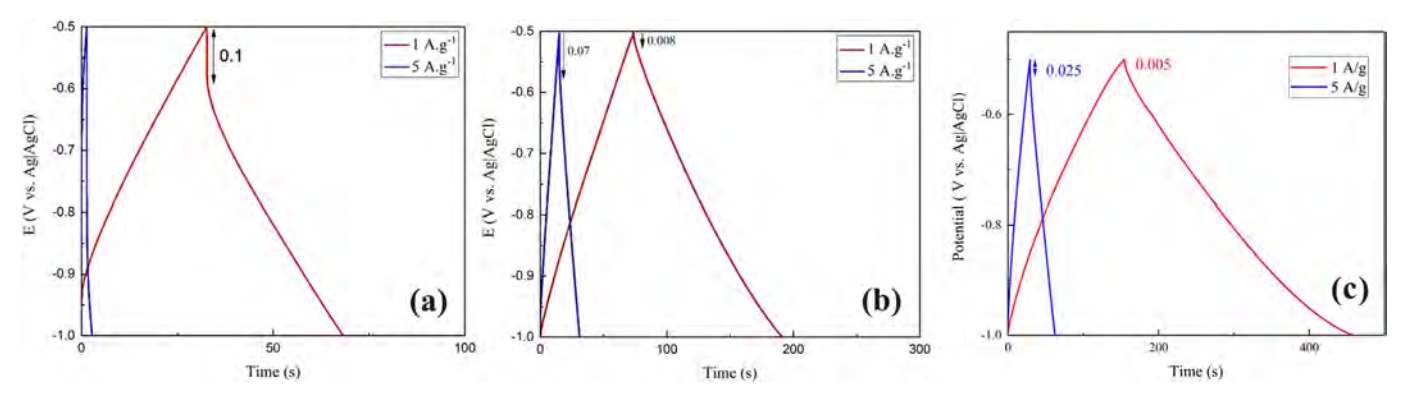


Fig. 14. GCD curves of a) GAS, b) GAL and c) GASL at current densities of 1-5 A/g.

Table 5 Specific capacitance (Cs) of samples at current densities of 5 Ag^{-1} and 1 Ag^{-1} . Capacitance retention is measured by increasing the current density.

Sample	Cs (1 Ag ⁻¹)	Cs (5 Ag ⁻¹)	[Cs (5 Ag ⁻¹)/Cs (1 Ag ⁻¹)]*100
GAS GAL	39 79	31 66	79 83
GASL	165	150	90

semicircle's diameter for the GASL sample. This low value is a consequence of high porosities in the structure which provides a better opportunity for redox reduction. GAS has a higher $\rm R_{ct}$ due to the lower level of reduction and highly aggregated sheets structure. This parameter is enhanced by using LAA which can cross-link the graphene sheets to hinder the aggregation and increase the porosity of structure. The utilization of both reducing agents causes the synergistic effect of microstructure and reduction of graphene aerogel that provides better electrochemical properties for the GASL sample.

Table 7 contains the internal resistance values compared to the other researches to introduce the present synthesis method as an effective route for electrochemical properties [20,51].

4. Conclusion

In summary, we introduced a new reduction media for the preparation of graphene aerogels via a mild chemical reduction process. The defined reducing system consists of L-AA and $NaHSO_3$ in equal mass ratio

FTIR analysis showed that reduction efficiency is enhanced due to the synergistic effect of the combined reducing system. The proposed mechanism for the reduction process indicated the role of $NaHSO_3$ in the improvement of the de-epoxidation step. Besides, L-AA can provide the cross-linking effect to impede the aggregation of graphene sheets, which is demonstrated in TEM and SEM images. XRD analysis showed the high-intensity peak of graphene aerogel is gained in the GASL sample because of highly reduced graphene sheets.

 N_2 adsorption analysis showed that the BET specific surface area and pore volume of the GASL sample are 135 m^2g^{-1} and 2.9 cm^3g^{-1} , respectively. The meso/macro pore-structure enhances the mobility of the ions by increasing the diffusion rate, which is favorable for electrode materials in the electrochemical capacitors.

The GASL sample demonstrated superior electrochemical performance in comparison with other samples synthesized via a single reducing agent. The CV analysis performed on GASL resulted in well-shaped rectangular curves, even at high scan rates. The capacitance retention reached 91% after 1000 cycles of charge/discharge and the specific capacitance was calculated 165 Fg $^{-1}$. Moreover, the low charge transfer resistance (about 0.2 Ω) measured in the EIS test, was contributed to the increment in porosity volume and the high electrical conductivity (3.6 Sm $^{-1}$). As a consequence, the utilized reducing system can be a basis for the preparation of various graphene-based nanocomposites for energy storage systems.

Compliance with etshical standards

This study wasn't funded and the authors declare that they have no conflict of interest.

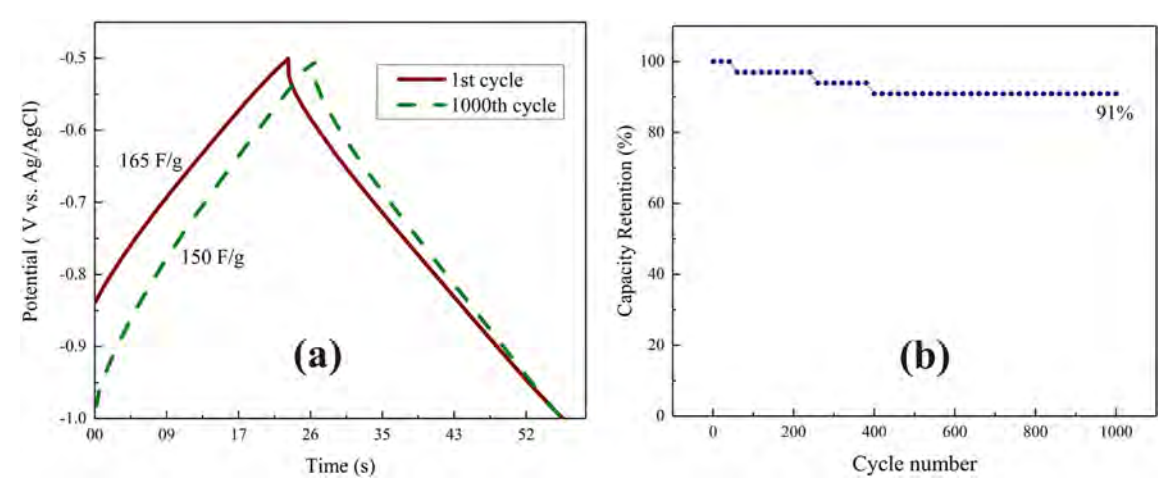


Fig. 15. a) GCD curves of GASL sample at 1 Ag⁻¹ after 1000cycles and b) capacity retention of GASL after 1000 cycles charge/discharge test.

Table 6Comparison of specific capacitance data of related studies.

Material	Specific capacitance (F g ⁻¹)	Electrolyte	Ref.
Graphene aerogel (GASL)	165	2 М КОН	This work
resorcinol-formaldehyde derived carbon aerogel	45	Aqueous electrolyte	[41]
Chemically reduced GO	135	Aqueous KOH	[42]
•	99	Organic electrolyte	
Thermal reduction in propylene carbonate	120	Organic electrolyte	[43]
MnO ₂ nanowire–graphene	117	H ₂ SO ₄	[44]
	31	Neutral aqueous Na ₂ SO ₄	
Graphene/CNT aerogel-NF	142	6 М КОН	[45]
Ti3C2Tx/MoO ₃	151	1 M KOH	[46]
Ti3C2Tx/ZnO	120	1 M KOH	[47]
3D graphene framework	113.2	6 М КОН	[48]
3D graphene monolith	~80	1 M lithium hexafluorophosphate	[49]
carbon nanotubes (CNTs) onto carbon fiber (CF)	143	1 M H ₂ SO ₄	[50]

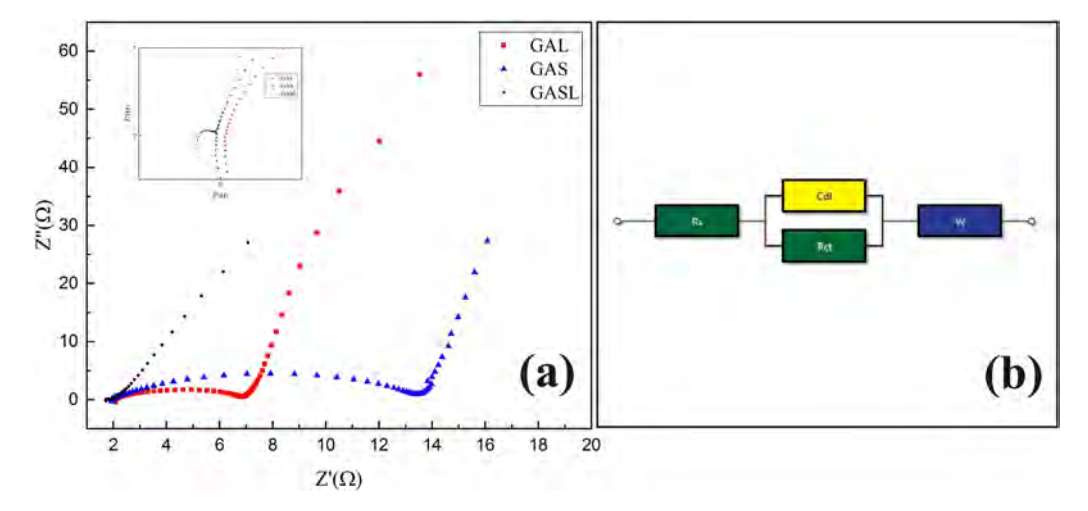


Fig. 16. Nyquist plots GAS, GAL and GASL samples, and the equivalent Randles circuit.

Table 7Comparison of EIS data in related studies.

Material	The resistance of solution (Ω)	$R_{ct}(\Omega)$	Ref.
Graphene aerogel (GASL)	1.7	0.2	In this work
Graphene aerogel/ZnO and Co ₃ O ₄	1.3	4.3	[20]
Graphene aerogel	_	3.6	[52]
MnO ₂ @CNTs@3DGA	_	8.5	[53]
rGO/CNT	_	2	[54]
MnO ₂ /3D CNTs-Graphene/Cu	_	0.23	[21]
Reduced graphene hydrogels	0.73	3.20	[55]
CoCO ₃ /GA	6.5	146.9	[25]
Co ₃ O ₄ /GA	10.9	97.5	

Declaration of competing interest

The authors declare that they have no known competing financial interests or personal relationships that could have appeared to influence the work reported in this paper.

Acknowledgments

This research did not receive any specific grant from funding agencies in the public, commercial, or not-for-profit sectors.

References

- [1] V. Chabot, D. Higgins, A. Yu, X. Xiao, Z. Chen, J. Zhang, A review of graphene and graphene oxide sponge: material synthesis and applications to energy and the environment, Energy Environ. Sci. 7 (2014) 1564–1596, https://doi.org/10.1039/ c3ee43385d.
- [2] C. Chen, X. Zhu, B. Chen, Covalently cross-linked graphene oxide aerogel with stable structure for high-efficiency water purification, Chem. Eng. J. 354 (2018) 896–904, https://doi.org/10.1016/j.cej.2018.08.034.
- [3] F. Tavakoli, M. Salavati-Niasari, A. Badiei, F. Mohandes, Green synthesis and characterization of graphene nanosheets, Mater. Res. Bull. 63 (2015) 51–57, https://doi.org/10.1016/j.materresbull.2014.11.045.
- [4] H. Maleki, Recent advances in aerogels for environmental remediation applications: a review, Chem. Eng. J. 300 (2016) 98–118, https://doi.org/10.1016/j.cej.2016.04. 098
- [5] K. Hu, X. Xie, T. Szkopek, M. Cerruti, Understanding hydrothermally reduced graphene oxide hydrogels: from reaction products to hydrogel properties, Chem. Mater. 28 (2016) 1756–1768, https://doi.org/10.1021/acs.chemmater.5b04713.
- [6] G. Gorgolis, C. Galiotis, Graphene aerogels: a review, 2D Mater. 4 (2017) 32001, https://doi.org/10.1088/2053-1583/aa7883.
- [7] I.K. Moon, J. Lee, R.S. Ruoff, H. Lee, Reduced graphene oxide by chemical graphitization, Nat. Commun. 1 (2010) 1–6, https://doi.org/10.1038/ncomms1067.
- [8] S. Pei, H.-M. Cheng, The reduction of graphene oxide, Carbon N. Y. 50 (2012) 3210–3228, https://doi.org/10.1016/j.carbon.2011.11.010.
- [9] H. Nosrati, R.S. Mamoory, F. Dabir, M.C. Perez, M.A. Rodriguez, D.Q. Svend Le, C.E. Bünger, In situ synthesis of three dimensional graphene-hydroxyapatite nano powders via hydrothermal process, Mater. Chem. Phys. 222 (2019) 251–255, https://doi.org/10.1016/j.matchemphys.2018.10.023.
- [10] H. Nosrati, R.S. Mamoory, F. Dabir, D.Q. Svend Le, C.E. Bünger, M.C. Perez, M.A. Rodriguez, Effects of hydrothermal pressure on in situ synthesis of 3D graphene- hydroxyapatite nano structured powders, Ceram. Int. 45 (2019) 1761–1769, https://doi.org/10.1016/j.ceramint.2018.10.059.
- [11] A. Salehabadi, M. Salavati-Niasari, M. Ghiyasiyan-Arani, Self-assembly of hydrogen storage materials based multi-walled carbon nanotubes (MWCNTs) and Dy3Fe5O12 (DFO) nanoparticles, J. Alloys Compd. 745 (2018) 789–797, https://doi.org/10. 1016/j.jallcom.2018.02.242.
- [12] W. Chen, L. Yan, P.R. Bangal, Chemical reduction of graphene oxide to graphene by sulfur-containing compounds, J. Phys. Chem. C 114 (2010) 19885–19890, https://

- doi.org/10.1021/jp107131v.
- [13] B. Zhang, J. Zhang, X. Sang, C. Liu, T. Luo, L. Peng, B. Han, X. Tan, X. Ma, D. Wang, N. Zhao, Cellular graphene aerogel combines ultralow weight and high mechanical strength: a highly efficient reactor for catalytic hydrogenation, Sci. Rep. 6 (2016) 25830, https://doi.org/10.1038/srep25830.
- [14] W. Chen, L. Yan, In situ self-assembly of mild chemical reduction graphene for three-dimensional architectures, Nanoscale 3 (2011) 3132–3137, https://doi.org/ 10.1039/c1nr10355e.
- [15] A. Navaee, A. Salimi, Efficient amine functionalization of graphene oxide through the Bucherer reaction: an extraordinary metal-free electrocatalyst for the oxygen reduction reaction, RSC Adv. 5 (2015) 59874–59880, https://doi.org/10.1039/ c5ra07892i
- [16] J. Zhang, H. Yang, G. Shen, P. Cheng, J. Zhang, S. Guo, Reduction of graphene oxide via ascorbic acid, Chem. Commun. 46 (2010) 1112–1114, https://doi.org/10.1039/ R917705A
- [17] C.K. Chua, M. Pumera, Chemical reduction of graphene oxide: a synthetic chemistry viewpoint, Chem. Soc. Rev. 43 (2014) 291–312, https://doi.org/10.1039/ c3cs60303b
- [18] C. Xiong, B. Li, X. Lin, H. Liu, Y. Xu, J. Mao, C. Duan, T. Li, Y. Ni, The recent progress on three-dimensional porous graphene-based hybrid structure for supercapacitor, Compos. B Eng. 165 (2019) 10–46, https://doi.org/10.1016/j.compositesb.2018.11.085.
- [19] X. Li, Y. Tang, J. Song, W. Yang, M. Wang, C. Zhu, W. Zhao, J. Zheng, Y. Lin, Self-supporting activated carbon/carbon nanotube/reduced graphene oxide flexible electrode for high performance supercapacitor, Carbon N. Y. 129 (2018) 236–244, https://doi.org/10.1016/j.carbon.2017.11.099.
- [20] A. Ghazitabar, M. Naderi, D. Fatmehsari Haghshenas, M. Rezaei, Synthesis of N-doped graphene aerogel/Co3O4/ZnO ternary nanocomposite via mild reduction method with an emphasis on its electrochemical characteristics, J. Alloys Compd. 794 (2019) 625–633, https://doi.org/10.1016/j.jallcom.2019.04.188.
- [21] T. Bi, H. Fang, J. Jiang, X.X. He, X. Zhen, H. Yang, Z. Wei, Z. Jia, Enhance super-capacitive performance of MnO2/3D carbon nanotubes-graphene as a binder-free electrode, J. Alloys Compd. 787 (2019) 759–766, https://doi.org/10.1016/j.jallcom.2019.02.117.
- [22] H. Gholipour-Ranjbar, M.R. Ganjali, P. Norouzi, H.R. Naderi, Synthesis of cross-linked graphene aerogel/Fe2O3 nanocomposite with enhanced supercapacitive performance, Ceram. Int. 42 (2016) 12097–12104, https://doi.org/10.1016/j.ceramint.2016.04.140.
- [23] Y. Zhou, L. Wen, K. Zhan, Y. Yan, B. Zhao, Three-dimensional porous graphene/ nickel cobalt mixed oxide composites for high-performance hybrid supercapacitor, Ceram. Int. 44 (2018) 21848–21854, https://doi.org/10.1016/j.ceramint.2018.08. 292
- [24] S. Ren, P. Rong, Q. Yu, Preparations, properties and applications of graphene in functional devices: a concise review, Ceram. Int. 44 (2018) 11940–11955, https:// doi.org/10.1016/j.ceramint.2018.04.089.
- [25] M.A. Garakani, S. Abouali, B. Zhang, C.A. Takagi, Z.L. Xu, J.Q. Huang, J. Huang, J.K. Kim, Cobalt carbonate/and cobalt oxide/graphene aerogel composite anodes for high performance li-ion batteries, ACS Appl. Mater. Interfaces 6 (2014) 18971–18980, https://doi.org/10.1021/am504851s.
- [26] M. Masjedi-Arani, M. Salavati-Niasari, Novel synthesis of Zn2GeO4/graphene nanocomposite for enhanced electrochemical hydrogen storage performance, Int. J. Hydrogen Energy 42 (2017) 17184–17191, https://doi.org/10.1016/j.ijhydene. 2017.05.118.
- [27] N. binti Hamzan, M.M. bin Ramly, N.M. Huang, S.A. Rahman, B.T. Goh, Growth of high density NiSi/SiC core-shell nanowires by hot-wire chemical vapour deposition for electrochemical applications, Mater. Char. 132 (2017) 187–198, https://doi. org/10.1016/j.matchar.2017.08.005.
- [28] A. Ghazitabar, M. Naderi, D. Fatmehsari Haghshenas, A facile chemical route for synthesis of nitrogen-doped graphene aerogel decorated by Co3O4 nanoparticles, Ceram. Int. 44 (2018) 23162–23171, https://doi.org/10.1016/j.ceramint.2018.09
- [29] W. Zhang, J. Chen, Y. Hu, Z. Fang, J. Cheng, Y. Chen, Adsorption characteristics of tetrabromobisphenol A onto sodium bisulfite reduced graphene oxide aerogels, Colloids Surfaces A Physicochem. Eng. Asp. 538 (2018) 781–788, https://doi.org/ 10.1016/j.colsurfa.2017.11.070.
- [30] M. Masjedi-Arani, M. Salavati-Niasari, Novel synthesis of Zn2GeO4/graphene nanocomposite for enhanced electrochemical hydrogen storage performance, Int. J. Hydrogen Energy 42 (2017) 17184–17191, https://doi.org/10.1016/j.ijhydene. 2017 05 118
- [31] H. Safajou, H. Khojasteh, M. Salavati-Niasari, S. Mortazavi-Derazkola, Enhanced photocatalytic degradation of dyes over graphene/Pd/TiO2 nanocomposites: TiO2 nanowires versus TiO2 nanoparticles, J. Colloid Interface Sci. 498 (2017) 423–432, https://doi.org/10.1016/j.jcis.2017.03.078.
- [32] H. Safardoust-Hojaghan, M. Salavati-Niasari, Degradation of methylene blue as a pollutant with N-doped graphene quantum dot/titanium dioxide nanocomposite, J. Clean. Prod. 148 (2017) 31–36, https://doi.org/10.1016/j.jclepro.2017.01.169.
- [33] R. Castaldo, G.C. Lama, P. Aprea, G. Gentile, M. Lavorgna, V. Ambrogi, P. Cerruti, Effect of the oxidation degree on self-assembly, adsorption and barrier properties of

- nano-graphene, Microporous Mesoporous Mater. 260 (2018) 102–115, https://doi.org/10.1016/j.micromeso.2017.10.026.
- [34] M. Mahdiani, F. Soofivand, F. Ansari, M. Salavati-Niasari, Grafting of CuFe12019 nanoparticles on CNT and graphene: eco-friendly synthesis, characterization and photocatalytic activity, J. Clean. Prod. 176 (2018) 1185–1197, https://doi.org/10. 1016/i.jclepro.2017.11.177.
- [35] H. Khojasteh, M. Salavati-Niasari, H. Safajou, H. Safardoust-Hojaghan, Facile reduction of graphene using urea in solid phase and surface modification by N-doped graphene quantum dots for adsorption of organic dyes, Diam. Relat. Mater. 79 (2017) 133–144, https://doi.org/10.1016/j.diamond.2017.09.011.
- [36] F. Mohandes, M. Salavati-Niasari, Freeze-drying synthesis, characterization and in vitro bioactivity of chitosan/graphene oxide/hydroxyapatite nanocomposite, RSC Adv. 4 (2014) 25993–26001, https://doi.org/10.1039/c4ra03534h.
- [37] G. Xiong, H. Luo, G. Zuo, K. Ren, Y. Wan, Novel Porous Graphene Oxide and Hydroxyapatite Nanosheets-Reinforced Sodium Alginate Hybrid Nanocomposites for Medical Applications, Elsevier Inc., 2015, https://doi.org/10.1016/j.matchar. 2015.07.016
- [38] S. Barg, F.M. Perez, N. Ni, P. Do Vale Pereira, R.C. Maher, E. Garcia-Tuñon, S. Eslava, S. Agnoli, C. Mattevi, E. Saiz, Mesoscale assembly of chemically modified graphene into complex cellular networks, Nat. Commun. 5 (2014) 4328, https:// doi.org/10.1038/ncomms5328.
- [39] D. Wu, T. Wang, L. Wang, D. Jia, Hydrothermal synthesis of nitrogen, sulfur co-doped graphene and its high performance in supercapacitor and oxygen reduction reaction, Microporous Mesoporous Mater. 290 (2019) 109556, https://doi.org/10.1016/j.micromeso.2019.06.018.
- [40] J. Wu, X.Z. Yuan, H. Wang, Cyclic voltammetry, PEM Fuel Cell Diagnostic Tools 60 (2011) 71–85, https://doi.org/10.1201/b11100-6.
- [41] A.C. Pierre, G.M. Pajonk, Chemistry of aerogels and their applications, Chem. Rev. 102 (2002) 4243–4266, https://doi.org/10.1021/cr0101306.
- [42] C.W. Chang, Y.C. Liao, Accelerated sedimentation velocity assessment for nanowires stabilized in a non-Newtonian fluid, Langmuir 32 (2016) 13620–13626, https://doi.org/10.1021/acs.langmuir.6b03602.
- [43] Y. Zhu, M.D. Stoller, W. Cai, A. Velamakanni, R.D. Piner, D. Chen, R.S. Ruoff, Exfoliation of graphite oxide in propylene carbonate and thermal reduction of the resulting graphene oxide platelets, ACS Nano 4 (2010) 1227–1233, https://doi.org/ 10.1021/nn901689k.
- [44] Z.S. Wu, W. Ren, D.W. Wang, F. Li, B. Liu, H.M. Cheng, High-energy MnO2 nano-wire/graphene and graphene asymmetric electrochemical capacitors, ACS Nano 4 (2010) 5835–5842, https://doi.org/10.1021/nn101754k.
- [45] S. Ye, J. Feng, P. Wu, Deposition of three-dimensional graphene aerogel on nickel foam as a binder-free supercapacitor electrode, ACS Appl. Mater. Interfaces 5 (2013) 7122–7129, https://doi.org/10.1021/am401458x.
- [46] J. Zhu, X. Lu, L. Wang, Synthesis of a MoO 3/Ti 3 C 2 T: X composite with enhanced capacitive performance for supercapacitors, RSC Adv. 6 (2016) 98506–98513, https://doi.org/10.1039/c6ra15651g.
- [47] F. Wang, M. Cao, Y. Qin, J. Zhu, L. Wang, Y. Tang, ZnO nanoparticle-decorated twodimensional titanium carbide with enhanced supercapacitive performance, RSC Adv. 6 (2016) 88934–88942, https://doi.org/10.1039/c6ra15384d.
- [48] L. Wu, W. Li, P. Li, S. Liao, S. Qiu, M. Chen, Y. Guo, Q. Li, C. Zhu, L. Liu, Powder, paper and foam of few-layer graphene prepared in high yield by electrochemical intercalation exfoliation of expanded graphite, Small 10 (2014) 1421–1429, https://doi.org/10.1002/smll.201302730.
- [49] K. Liu, Y.M. Chen, G.M. Policastro, M.L. Becker, Y. Zhu, Three-Dimensional bicontinuous graphene monolith from polymer templates, ACS Nano 9 (2015) 6041–6049, https://doi.org/10.1021/acsnano.5b01006.
- [50] M.S. Islam, Y. Deng, L. Tong, S.N. Faisal, A.K. Roy, A.I. Minett, V.G. Gomes, Grafting carbon nanotubes directly onto carbon fibers for superior mechanical stability: towards next generation aerospace composites and energy storage applications, Carbon N. Y. 96 (2016) 701–710, https://doi.org/10.1016/j.carbon.2015.10.002.
- [51] M. Foroutan, L. Naji, Systematic evaluation of factors influencing electrochemical and morphological characteristics of free-standing 3D graphene hydrogels as electrode material for supercapacitors, Electrochim. Acta 301 (2019) 421–435, https:// doi.org/10.1016/j.electacta.2019.01.161.
- [52] S.M. Jung, D.L. Mafra, C. Te Lin, H.Y. Jung, J. Kong, Controlled porous structures of graphene aerogels and their effect on supercapacitor performance, Nanoscale 7 (2015) 4386–4393, https://doi.org/10.1039/c4nr07564a.
- [53] Z. Pan, M. Liu, J. Yang, Y. Qiu, W. Li, Y. Xu, X. Zhang, Y. Zhang, High electroactive material loading on a carbon Nanotube@3D graphene aerogel for high-performance flexible all-solid-state asymmetric supercapacitors, Adv. Funct. Mater. 27 (2017) 1701122, https://doi.org/10.1002/adfm.201701122.
- [54] Z.D. Huang, B. Zhang, S.W. Oh, Q. Bin Zheng, X.Y. Lin, N. Yousefi, J.K. Kim, Self-assembled reduced graphene oxide/carbon nanotube thin films as electrodes for supercapacitors, J. Mater. Chem. 22 (2012) 3591–3599, https://doi.org/10.1039/c2im15048d.
- [55] J. Zhang, H. Cui, S.-F. Hou, J. Zhou, S. Zhuo, W. Si, J.-L. Zhang, L.-B. Xing, Three dimensional reduced graphene hydrogels with tunable pore sizes using thiourea dioxide for electrode materials in supercapacitors, Electrochim. Acta 176 (2015) 1288–1295, https://doi.org/10.1016/j.electacta.2015.07.150.